Carbon 100 (2016) 137–144

Contents lists available at ScienceDirect

Carbon

journal homepage: www.elsevier.com/locate/carbon

Strategy for yolk-shell structured metal oxide-carbon composite powders and their electrochemical properties for lithium-ion batteries

Hyeon Seok Ju, Young Jun Hong, Jung Sang Cho, Yun Chan Kang*

Department of Materials Science and Engineering, Korea University, Anam-Dong, Seongbuk-Gu, Seoul 136-713, Republic of Korea

ARTICLE INFO

Article history:
Received 30 March 2015
Received in revised form
10 November 2015
Accepted 3 January 2016
Available online 6 January 2016

Keywords:
Yolk-shell
Carbon composite
Lithium ion battery
Spray pyrolysis

ABSTRACT

A strategy for the preparation of metal oxide-carbon composite powders with yolk-shell structure by simple spray pyrolysis is introduced. Mn–Sn–O–C composite powders with yolk-shell structure representing the first target material are prepared by one-pot spray pyrolysis and their formation mechanism is evaluated. Phase separation of polyvinylpyrrolidone (PVP), Sn, and Mn components during the drying stage of droplets plays a key role in the formation of yolk-shell structured composite powders. The repeated combustion and contraction processes of the dried powders under N_2 atmosphere produce the desired Mn–Sn–O–C composite powders with yolk-shell structure. The shell and core parts of the yolk-shell powders prepared directly by spray pyrolysis at 900 °C are MnO–Mn_2SnO_4–C and Sn–Mn_2SnO_4–C composites, respectively. The initial discharge capacities of the composite powders prepared at 700 and 900 °C at the current density of 1 A g^{-1} are 1058 and 1204 mA h g^{-1}, respectively. The discharge capacities of the composite powders prepared at 900 °C for the 2nd and 100th cycle are 803 and 784 mA h g^{-1}, respectively. The structural stability of the Mn–Sn–O–C composite powders with yolk-shell structure during cycling results in good electrochemical performance.

1. Introduction

Yolk-shell or rattle-type structures, which are hybrids of core–shell and hollow structures with a distinctive core@void@shell configuration, have attracted tremendous interest in recent years owing to their unique characteristics that cannot be obtained in conventional materials [1–30]. Yolk-shell materials with homogeneous (MO_x@MO_x) and heterogeneous (MO_x@NO_x) structures have been developed over a wide range of compositions for a large variety of applications including energy storage [5–25]. Especially, various yolk-shell materials for lithium-ion batteries (LIBs) have been developed by various methods including hydrothermal, spray-pyrolysis, and spray-drying processes [6–27]. Carbon materials, such as amorphous carbon, carbon nanotubes, and graphene, have been applied to form nanostructured metal oxide-C composite materials with good electrochemical properties [31–40]. Inclusion of carbon material improved the electrochemical properties of metal oxide materials by improving the structural stability during cycling and by increasing the electronic conductivity [31–40]. However, to the best of our knowledge, the preparation of metal oxide-carbon composite materials with yolk-shell structures, and their electrochemical properties when used as anode materials for LIBs have not been reported.

In the literature, yolk-shell materials have been mainly prepared by a step-by-step etching process or by thermal treatments applying Ostwald ripening or the Kirkendall effect [1–5]. Recently, combustion of metal oxide-carbon composite materials formed as intermediate product in spray-pyrolysis and spray-drying processes produced various types of yolk-shell materials [20–25]. However, these processes applied for the preparation of yolk-shell materials, as described in the literature, cannot be applied for the preparation of metal oxide-carbon composite materials with yolk-shell structure. Therefore, it still remains a challenge to develop a process for the fabrication of yolk-shell metal oxide-carbon composite powders, in which core and shell parts are metal oxide-carbon composites. In addition, synergistic effects of structural features and chemical composition of anode materials have to be achieved to develop anode materials with superior electrochemical properties for LIBs.

In this study, a strategy for the preparation of metal oxide-carbon composite powders with yolk-shell structure by simple spray pyrolysis is introduced. Manganese oxide (MnO) and tin

* Corresponding author. Fax: +82 2 928 3584.
E-mail address: yckang@korea.ac.kr (Y.C. Kang).

http://dx.doi.org/10.1016/j.carbon.2016.01.008
0008-6223/

oxide (SnO_2) have attracted great attention as anode materials for LIBs owing to their high theoretical capacities, low discharge–charge potentials, low costs, and environmental friendliness [17–19,41–43]. Therefore, Mn–Sn–O–C composite powders with yolk-shell structure representing the first target material were prepared by one-pot spray pyrolysis. The formation mechanism of the yolk-shell metal oxide-carbon composite powder was evaluated in detail by investigating the morphological changes of the powders during the spray pyrolysis depending on the preparation temperature. In addition, the electrochemical properties of the Mn–Sn–O–C composite powders with yolk-shell structure were investigated.

2. Experimental

2.1. Synthesis of the yolk-shell Mn–Sn–O–C composite

Mn–Sn–O–C composite powders with Sn/Mn mole ratio of 1:3 were prepared directly by ultrasonic spray pyrolysis from spray solution containing the carbon source material. The schematic diagram of the apparatus is shown in Fig. S1. A quartz reactor with length of 1200 mm and diameter of 50 mm was used. A 1.7-MHz ultrasonic spray generator with six vibrators was used to generate a large quantity of droplets. The total concentration of the Mn and Sn components dissolved in distilled water was 0.3 M. In this study, polyvinylpyrrolidone (PVP, M_w = 40,000) was used as carbon source material to prepare the Mn–Sn–O–C composite powders with yolk-shell structure. The amount of PVP dissolved in the spray solution of 250 mL was fixed at 10 g. The flow rate of N_2 used as carrier gas was fixed at 5 L min^{-1}. The reactor temperature during the spray pyrolysis process was changed from 300 to 900 °C.

2.2. Characterizations

The crystal structures of the resulting microspheres were investigated by X-ray diffractometry (XRD, X'pert PRO MPD) using Cu-Kα radiation (λ = 1.5418 Å). The morphologies of the microspheres were characterized using filed-emission scanning electron microscopy (FE-SEM, Hitachi S-4300) and high-resolution transmission electron microscopy (HR-TEM, JEM-2100F) operating at a working voltage of 200 kV. The specific surface areas of the powders were calculated by the Brunauer–Emmett–Teller (BET) analysis of nitrogen adsorption measurements (TriStar 3000). The carbon content of the Mn–Sn–O–C composite powders with yolk-shell structure was determined using thermogravimetric analysis (TGA, SDT Q600), which was performed in air at a heating rate of 10 °C min^{-1}.

2.3. Electrochemical measurements

The capacities and cycling properties of the Mn–Sn–O–C composite powders were determined using a 2032-type coin cell. The electrode was prepared from a mixture containing 70 wt% of active material, 20 wt% of activated carbon (Super P), and 10 wt% of sodium carboxymethyl cellulose (CMC) binder. Lithium metal and microporous polypropylene film were used as counter electrode and separator, respectively. The electrolyte was a solution of 1 M $LiPF_6$ and a mixture of fluoroethylene carbonate–dimethyl carbonate (FEC–DMC) at the volume ratio of 1:1. The charge/discharge characteristics of the samples were determined through cycling in the potential range of 0.001–3 V at various fixed current densities. Cyclic voltammetry (CV) measurements were carried out at the scan rate of 0.07 mV s^{-1}.

3. Results and discussion

The XRD patterns of the Mn–Sn–O–C composite powders prepared by spray pyrolysis at various temperatures are shown in Fig. 1. The composite powders prepared at 300 °C showed broad amorphous peaks without sharp crystalline reflections. However, crystalline peaks of Sn metal and the MnO phase were observed in the XRD pattern of the powders prepared at 500 °C. The XRD pattern of the powders prepared at 700 °C showed main peaks of Sn metal, MnO, and Mn_2SnO_4. The peak intensities of the Sn metal decreased at the preparation temperature of 900 °C, while the sharpness of the peaks of MnO and Mn_2SnO_4 increased.

Images of the morphologies and elemental mapping of the Mn–Sn–O–C composite powders prepared by spray pyrolysis at various temperatures are shown in Fig. 2–4. The SEM and TEM images of the powders prepared at the low temperature of 300 °C shown in Fig. 2 clearly reveal the core–shell structure. The dense core part corresponding to the white areas in the SEM image and dark areas in the TEM image was uniformly covered with material forming a porous shell. Powders with single cores were observed from the SEM and TEM images. The high resolution TEM image shown in Fig. 2d shows clear lattice fringes 0.49 and 0.26 nm apart, corresponding to the (200) and (111) crystal planes of MnO, respectively. The elemental-mapping image of the sample with single core is shown in Fig. 2e and revealed the distributions of Sn, Mn, C, and N over the composite powder. The Sn component was mainly observed in the single core part. However, Mn was observed in the core and shell parts of the powder. The size of the Mn-rich core part was slightly larger than that of the Sn-rich core part, as shown by the dotted lines in Fig. 2e. Therefore, we can estimate that the core part again had a core–shell sub-structure, in which Sn-related material is fully covered by Mn-related material. The C component originating from PVP was mainly observed in the shell part of the powder, as shown by the dotted circle. The distribution of N all over the powder revealed incomplete decomposition of PVP. The TEM images of the powders shown in Fig. S2 revealed melted and non-melted material. PVP is water soluble. Therefore, the spherical morphology of some specimens was destroyed by the dissolving of PVP into water during the sampling process of the powders on carbon-coated copper grid used for the TEM analysis. However, some of the samples maintained their spherical morphology even if dispersed in water. The partial decomposition

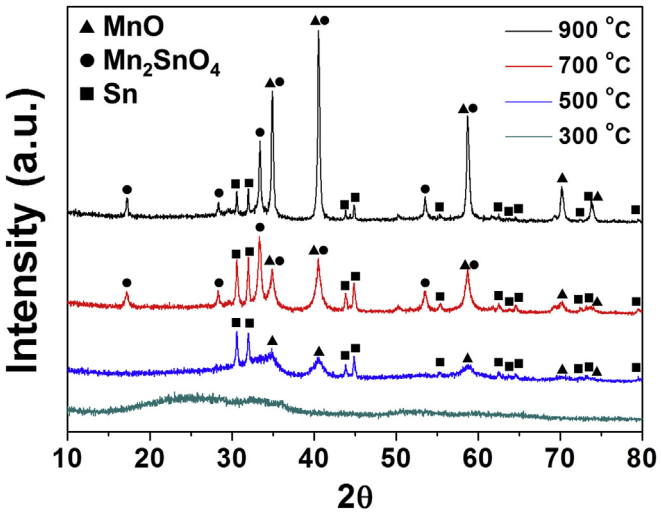

Fig. 1. - XRD patterns of the powders prepared by spray pyrolysis at various temperatures. (A color version of this figure can be viewed online.)

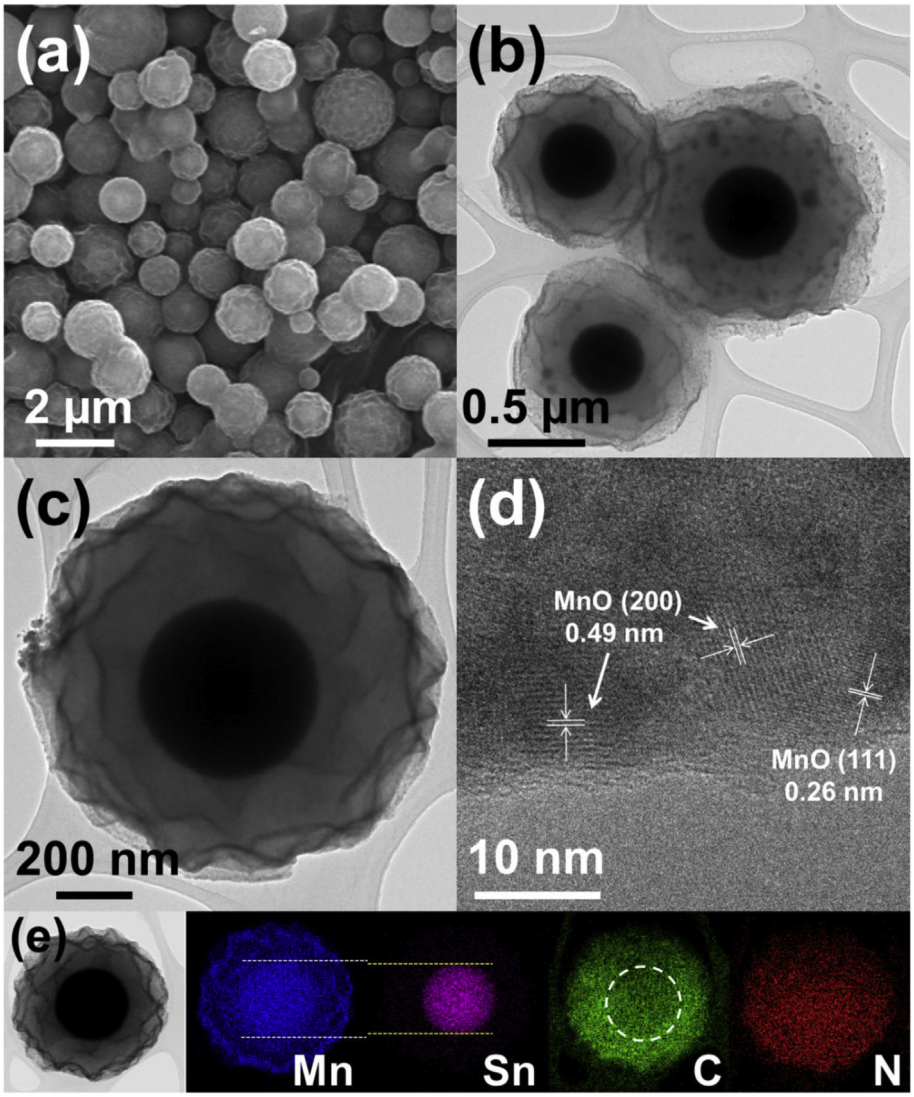

Fig. 2. - Morphologies and elemental mapping images of the powders prepared by spray pyrolysis at 300 °C: (a) SEM image, (b)–(d) TEM images, and (e) elemental mapping images. (A color version of this figure can be viewed online.)

of PVP into other carbon material occurred mainly at the surface of the powders. Energy dispersive X-ray analysis (EDXA) patterns of the powders shown in Fig. S3 also revealed the different compositions in dependence of the position. The Mn and C components were mainly detected near the surface.

The SEM and TEM images of the powders prepared at the temperature of 700 °C are shown in Fig. 3 and clearly revealed the yolk-shell structure. The void space between core and shell parts was observed in the TEM images. The core part shown in Fig. 3b and c again had a clear core–shell sub-structure, like the powders prepared at the temperature of 300 °C. The spherical single core was covered by an amorphous-like coating layer, as indicated by arrows in Fig. 3c. The elemental-mapping images shown in Fig. 3e also revealed the carbon coating layer covering the single core part consisting of Mn and Sn components, as shown by the dotted circle. The identical size of nanospheres representing the Mn and Sn components in the core part revealed the reaction of Mn and Sn to form Mn_2SnO_4, as also evidenced by the XRD pattern presented in Fig. 1. The small nanoparticles dispersed in the shell part of the powder were identified as Sn metal on the basis of the elemental-mapping images. The metallic Sn nanoparticles were dispersed within the hollow MnO–C composite shell layer. The high resolution TEM image shown in Fig. 3d shows clear lattice fringe 0.26 nm apart, corresponding to the (111) crystal plane of MnO. The powders prepared directly by spray pyrolysis at 900 °C had also a yolk-shell structure, as evidenced by the SEM and TEM images shown in Fig. 4a–c. However, the growth of crystalline MnO and Mn_2SnO_4 resulted in powders with rough surface. The high resolution TEM image shown in Fig. 4d shows clear lattice fringes 0.51 and 0.26 nm apart, corresponding to the (111) crystal planes of Mn_2SnO_4 and MnO, respectively. The elemental-mapping images shown in Fig. 4e revealed the uniform distribution of the Mn, Sn, and C components all over the yolk-shell powder. The uniform distributions of Mn and Sn in the shell part correspond to the formation of ultrafine crystals of Mn_2SnO_4 in the shell layer. Therefore, the XRD peak intensities of Sn metal in Fig. 1 decreased when the preparation temperature was increased from 700 to 900 °C. EDXA patterns of the powders shown in Figs. S4 and S5 revealed the different compositions in dependence of the position of the composite powders prepared at 700 and 900 °C. The composition and the surface electronic states of the Mn–Sn–O–C composite powders with yolk-shell structure prepared by spray pyrolysis at 900 °C were characterized by X-ray

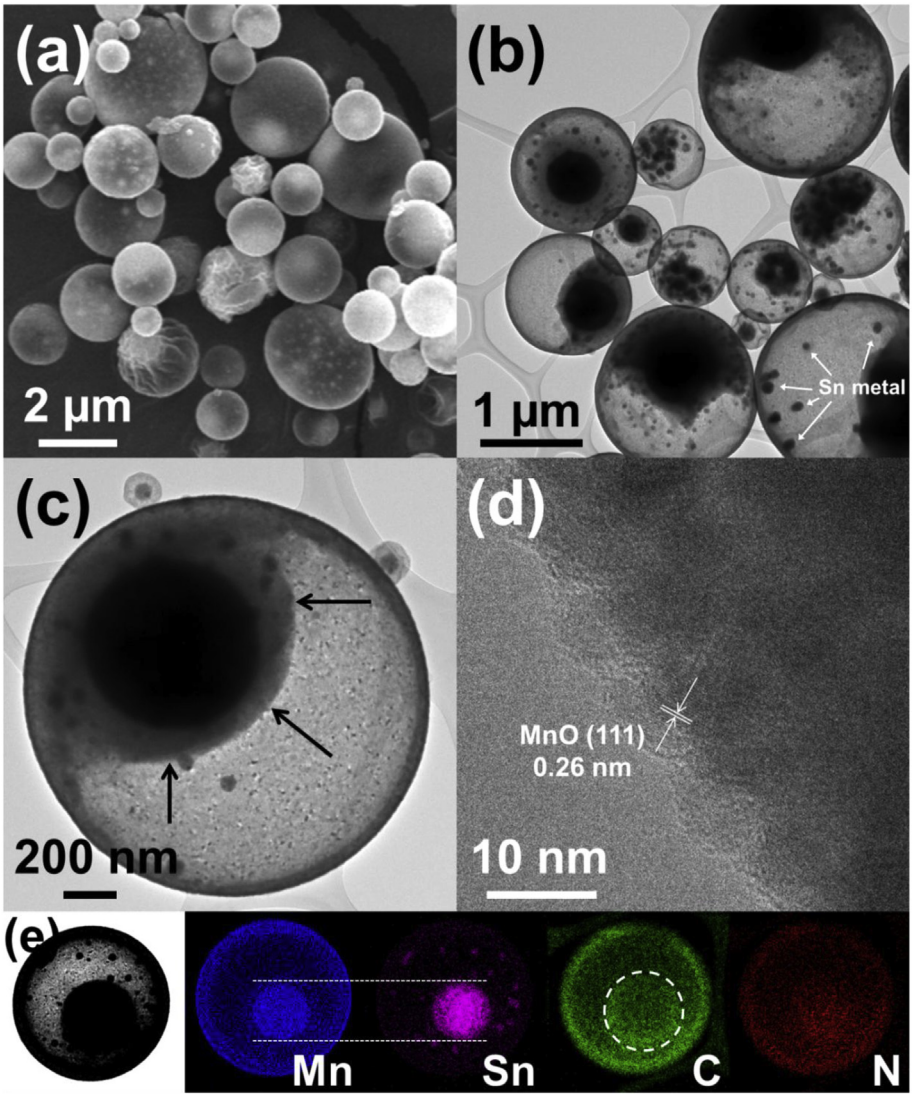

Fig. 3. - Morphologies and elemental mapping images of the powders prepared by spray pyrolysis at 700 °C: (a) SEM image, (b)–(d) TEM images, and (e) elemental mapping images. (A color version of this figure can be viewed online.)

photoelectron spectroscopy (XPS). The XPS survey spectrum in Fig. S6a of the Mn–Sn–O–C composite powders confirmed the presence of Mn, Sn, O, and C signals. In the Mn 2p spectrum of the Mn–Sn–O–C composite powders, shown in Fig. S6b, the main peaks observed occurred at binding energies of 653.2 eV for Mn $2p_{1/2}$ and 641.5 eV for Mn $2p_{3/2}$ [44]. Additionally, the binding energies of 486.5 eV for Sn $3d_{5/2}$ and 494.9 eV for Sn $3d_{3/2}$ were also observed from the Sn 3d spectrum (Fig. S6c) [45]. The C1s peaks shown in Fig. S6d could be attributed to sp^2-bonded carbon (C–C), epoxy and alkoxy groups (C–O), and carbonyl and carboxylic (C=O) groups, which correspond to peaks at 284.6, 285.8, and 288.1 eV, respectively [44]. The schematic structures of the powders prepared at 700 and 900 °C are shown in Scheme S1.

The formation mechanism of the Mn–Sn–O–C composite powders with yolk-shell structure is estimated from the morphological changes of the powders in dependence of the preparation temperature and can be inferred from Scheme 1. Phase separation of the PVP, Sn, and Mn components during the drying stage of the droplets resulted in core–shell powder with multiple shells. Melted Sn and Mn salts with high densities moved into the inner part of the powder to form the dense core. Sn salt was mainly located in the center part of the powder. Mn salt covered the Sn salt to form a core–shell structure. The porous shell part was a composite of PVP and Mn with small impurity of Sn salt. Some manganese ions were bound by strong ionic bonds to the amide groups of PVP [46,47]. Therefore, a part of the Mn component moved to the outside of the microsphere surrounded by PVP during the formation of core–shell structured powder with multiple shells. The carbonization of PVP and decomposition of Mn salt in the outer part of the composite microspheres formed the MnO-carbon layer with small impurity component of Sn covering the composite powder. The subsequent contraction of the inner PVP-metal salt part resulted in the composite powder with yolk-shell structure, in which the core was composed of PVP, Sn and Mn salts. The second carbonization of PVP and decomposition of the Sn and Mn salts formed SnO_x-MnO-C cores with multiple layers. The carbon material partly reduced tin oxide into Sn metal. The reaction of SnO_x and MnO formed the Mn_2SnO_4 core. The small amount of the Sn component dispersed in the shell part completely reacted with MnO to form the Mn_2SnO_4 phase. Finally, the shell part was a composite of MnO–Mn_2SnO_4–C, and the core part was a composite of Sn–Mn_2SnO_4–C with multiple layers.

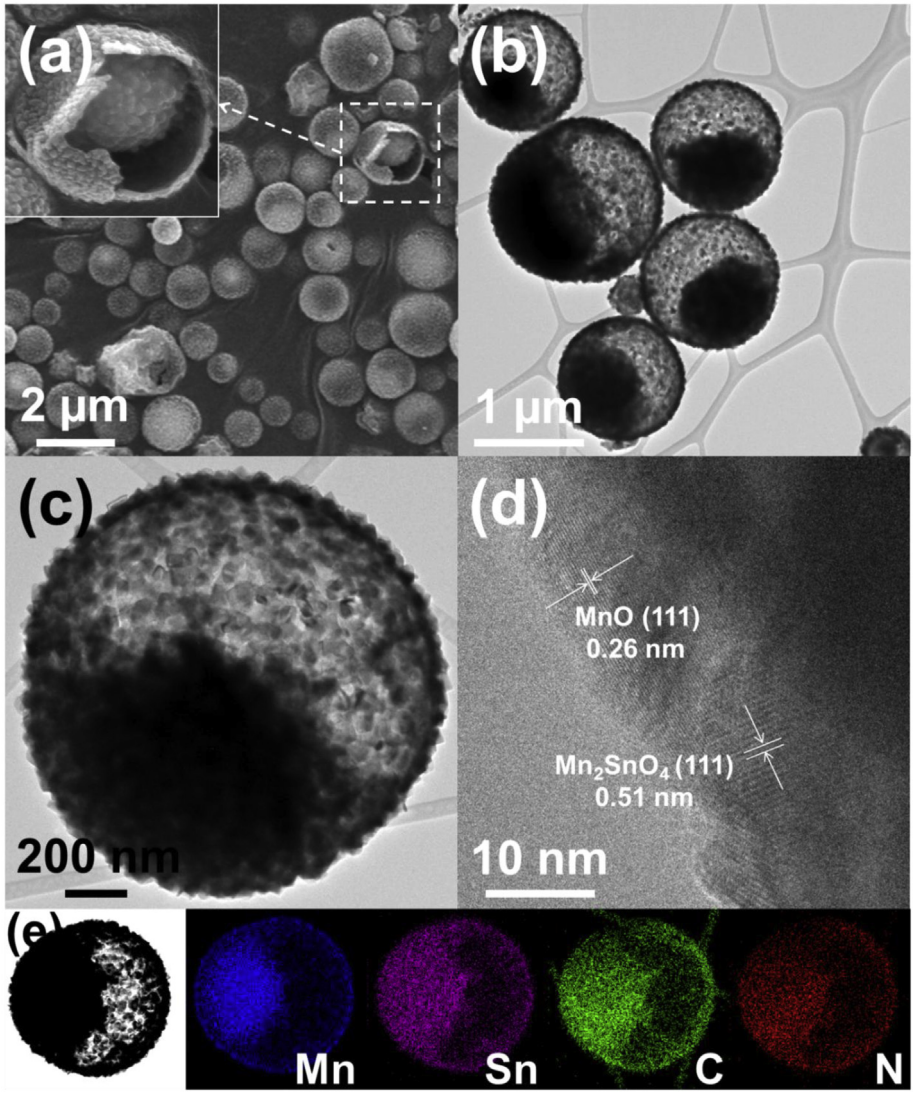

Fig. 4. - Morphologies and elemental mapping images of the powders prepared by spray pyrolysis at 900 °C: (a) SEM image, (b)–(d) TEM images, and (e) elemental mapping images. (A color version of this figure can be viewed online.)

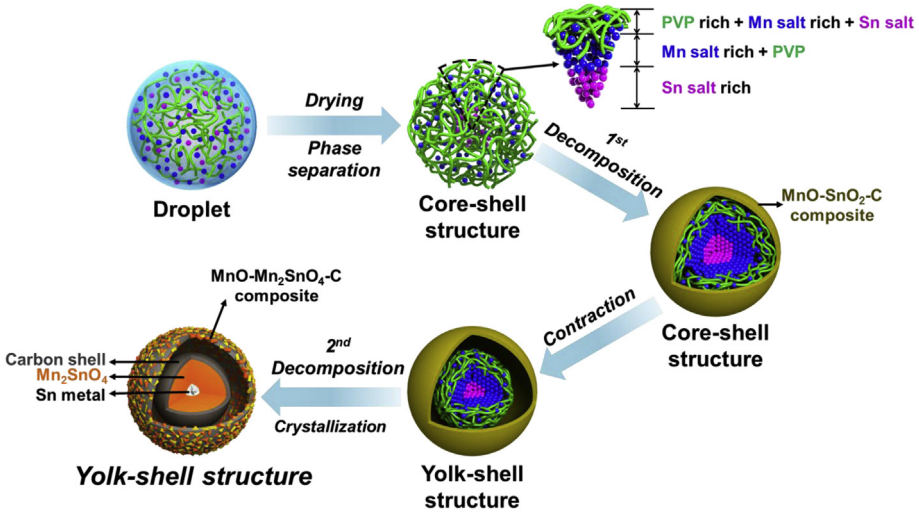

Scheme 1. - Formation mechanism of the Mn–Sn–O–C composite powders with yolk-shell structure.

The thermogravimetric (TG) curves of the composite powders prepared by spray pyrolysis at various temperatures are shown in Fig. S7. The composite powders prepared at the low temperature of 300 °C had three steps of weight losses at temperatures below 400 °C. The first weight loss observed at temperatures below 190 °C was attributed to the evaporation of adsorbed water molecules. The second and third weight-loss steps observed at around 190 and 250 °C were attributed to the carbonization of PVP and combustion of carbon, respectively. The weight loss of the composite powders prepared at temperatures above 500 °C mainly occurred by combustion of the carbon component. The slight weight increase of the powders prepared at the high temperature of 900 °C was ascribed to the oxidation of Sn metal to tin oxide. On the basis of the TGA results, the minimum carbon contents of the composite powders prepared at 500, 700 and 900 °C were 32, 24, and 8 wt%, respectively. The N_2 adsorption and desorption isotherms shown in Fig. S8 revealed the mesoporous structure of the Mn–Sn–O–C composite powders prepared at temperatures of 700 and 900 °C. The BET surface areas of the composite powders prepared at 500, 700, and 900 °C were 1.4, 49.0, and 48.0 $m^2\ g^{-1}$, respectively.

The CV curves of the Mn–Sn–O–C composite powders with yolk-shell structure prepared by spray pyrolysis at 900 °C were measured in the voltage range of 0.001–3.0 V vs. Li/Li^+ at a scan rate of 0.07 mV s^{-1} and are shown in Fig. 5a. The CV curve had four reduction peaks at around 1.0, 0.58, 0.42, and 0.02 V in the first discharging process. The broad reduction peak observed at around 1.0 V was attributed to the decomposition of Mn_2SnO_4 ($Mn_2SnO_4 + 4Li^+ + 4e^- \rightarrow 2MnO + 2Li_2O + Sn$) [48,49]. The sharp reduction peak at around 0.02 V was attributed to the alloying reaction between lithium and metallic Sn nanograins ($Sn + xLi^+ + xe^- \rightarrow Li_xSn$), conversion reaction of MnO to metallic Mn ($MnO + 2Li^+ + 2e^- \rightarrow Mn + Li_2O$), and formation of solid–electrolyte interface (SEI) layers in the first discharging process [48,49]. The multiple oxidation peaks observed between 0.6 and 0.8 V during the first charging process was attributed to the de-alloying reaction of Li_xSn compounds. The broad oxidation peak at around 1.25 V was attributed to the regeneration of the MnO phase ($Mn + Li_2O \rightarrow MnO + 2Li^+ + 2e^-$) and a slight decomposition of the SEI layers [48,49]. The reduction peaks shifted to the high voltage region from the second cycle onward due to the improved kinetics of the electrode forming ultrafine nanocrystals during the first discharging and charging processes [50,51]. The good overlapping of the CV curves starting from the second cycle indicated excellent electrochemical reversibility of the Mn–Sn–O–C composite powders with yolk-shell structure.

The initial charge and discharge curves of all investigated samples at the current density of 1 A g^{-1} are shown in Fig. 5b. The initial discharge capacities of the composite powders prepared at 500, 700, and 900 °C were 711, 1058, and 1204 mA h g^{-1}, and their corresponding initial Coulombic efficiencies were 40, 53, and 66%, respectively. The decrease of the initial discharge and charge capacities and initial Coulombic efficiencies of the composite powders with decreasing preparation temperature was due to the low capacity and high initial irreversible capacity loss of amorphous carbon material [52,53]. The cycling performances of the three samples at the current density of 1 A g^{-1} are shown in **Fig. 5**c. The Mn–Sn–O–C composite powders with yolk-shell structure had good cycling performances, irrespective of their preparation temperature. The discharge capacities of the composite powders prepared at 500, 700, and 900 °C for the 100th cycle were 370, 596, and 784 mA h g^{-1}, respectively. The volumetric capacity of the composite powders prepared at 900 °C for the 100th cycle was 447 mA h cm^{-3}. As shown in Fig. 5c, the composite powders prepared at 900 °C showed high Coulombic efficiencies of above 99% from the 7th cycle onward. The rate performance of the Mn–Sn–O–C composite powders with yolk-shell structure

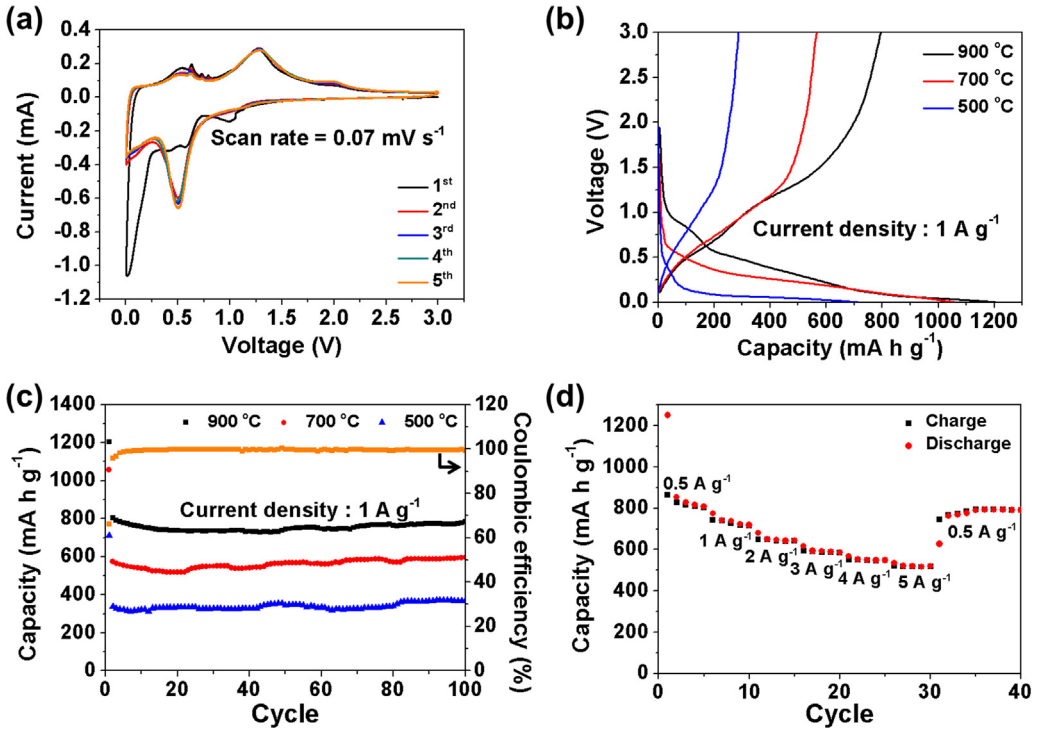

Fig. 5. Electrochemical properties of the powders prepared by spray pyrolysis at various temperatures: (a) CV curves of the powders prepared at 900 °C, (b) initial charge and discharge curves of the powders prepared at various temperatures, (c) cycling performances of the powders prepared at various temperatures, and (d) rate performance of the powders prepared at 900 °C. (A color version of this figure can be viewed online.)

prepared at 900 °C is shown in Fig. 5d, in which the current density was step-wise increased from 0.5 to 5 A g^{-1} and then returned to 0.5 A g^{-1} after 30 cycles. The stable discharge capacities of the composite powders at the current densities of 0.5, 1, 2, 3, 4, and 5 A g^{-1} were 826, 730, 654, 590, 550, and 519 mA h g^{-1}, respectively. The discharge capacity of the composite powders was well recovered after 30 cycles when the current density was returned to 0.5 A g^{-1}.

The Nyquist impedance plots of the Mn–Sn–O–C composite powders with yolk-shell structure prepared at 700 and 900 °C before and after 50th cycles are shown in Fig. 6. The medium-frequency semicircles in the Nyquist plots of the electrodes were assigned to the charge-transfer resistance (R_{ct}) [54,55]. The Mn–Sn–O–C composite powders with large crystallite size and low amount of carbon material had lower charge-transfer resistance than the composite powders with ultrafine crystallites and a high amount of carbon material, as shown in Fig. 6a. The low charge-transfer resistances of the two samples even after 50 cycles, as shown in Fig. 6b, revealed high structural stability of the Mn–Sn–O–C composite powders with yolk-shell structure during cycling and resulted in good cycling and rate performance. The morphologies of the Mn–Sn–O–C composite powders obtained after 100 cycles are shown in Fig. S9. The original yolk-shell structure of the Mn–Sn–O–C composite powders was perfectly maintained even after repeated lithium insertion and desertion processes. The long-term cycling performance of the Mn–Sn–O–C composite powders with yolk-shell structure prepared at 900 °C at the high current density of 5 A g^{-1} is shown in Fig. S10. The discharge capacities of the Mn–Sn–O–C composite powders increased steeply during the first 57 cycles due to the gradual activation of the composite powders at the high current density of 5 A g^{-1}. The discharge capacity of the composite powders for the 1000th cycle was 510 mA h g^{-1}.

4. Conclusions

In this study, metal oxide-carbon composite powders with yolk-shell structure were prepared by a one-pot spray-pyrolysis process. PVP used as carbon source material enabled the formation of composite powders with yolk-shell structure. The Mn–Sn–O–C composite powders with yolk-shell structure showed good cycling and rate performances when used as anode material for LIBs. The composite powders with a low carbon content of 8 wt% and prepared directly by spray pyrolysis at 900 °C had the best electrochemical performance. The new strategy employed in this study could be applied for the preparation of metal oxide-carbon composite materials with various compositions for a wide range of applications including energy storage.

Acknowledgment

This work was supported by the National Research Foundation of Korea (NRF) grant funded by the Korea government (MEST) (No. 2012R1A2A2A02046367).

Appendix A. Supplementary data

Supplementary data related to this article can be found at http://dx.doi.org/10.1016/j.carbon.2016.01.008.

References

[1] X.W. Lou, L. Archer, Z. Yang, Hollow micro-/nanostructures: synthesis and applications, Adv. Mater 20 (2008) 3987–4019.
[2] Y. Zhao, L. Jiang, Hollow micro/nanomaterials with multilevel interior structures, Adv. Mater 21 (2009) 3621–3638.
[3] J. Liu, S. Qiao, J. Chen, X. Lou, X. Xing, G. Lu, Yolk/shell nanoparticles : new platforms for nanoreactors, drug delivery and lithium-ion batteries, Chem. Commun. 47 (2011) 12578–12591.
[4] H. Wu, J. Chen, H. Hng, X. Lou, Nanostructured metal oxide-based materials as advanced anodes for lithium-ion batteries, Nanoscale 4 (2012) 2526–2542.
[5] J. Liu, H. Xia, D. Xue, L. Lu, Double-shelled nanocapsules of V_2O_5-based composites as high-performance anode and cathode materials for Li ion batteries, J. Am. Chem. Soc. 131 (2009) 12086–12087.
[6] X. Wang, X. Wu, Y. Guo, Y. Zhong, X. Cao, Y. Ma, J. Yao, Synthesis and lithium storage properties of Co3O4 nanosheet-assembled multishelled hollow spheres, Adv. Funct. Mater 20 (2010) 1680–1686.
[7] W. Zhao, H. Chen, Y. Li, L. Li, M. Lang, J. Shi, Uniform rattle-type hollow magnetic mesoporous spheres as drug delivery carriers and their sustained-release property, Adv. Funct. Mater 18 (2008) 2780–2788.
[8] G. Zhang, L. Yu, H. Wu, H. Hoster, X. Lou, Formation of $ZnMn_2O_4$ ball-in-ball hollow microspheres as a high-performance anode for lithium-ion batteries, Adv. Mater 24 (2012) 4609–4613.
[9] Z. Wang, L. Zhou, X. Lou, Metal oxide hollow nanostructures for lithium-ion batteries, Adv. Mater 24 (2012) 1903–1911.
[10] L. Zhou, D. Zhao, X. Lou, Double-shelled $CoMn_2O_4$ hollow microcubes as high-capacity anodes for lithium-ion batteries, Adv. Mater 24 (2012) 745–748.
[11] N. Liu, H. Wu, M. McDowell, Y. Yao, C. Wang, Y. Cui, A yolk-shell design for stabilized and scalable li-ion battery alloy anodes, Nano Lett. 12 (2012) 3315–3321.
[12] W. Cho, Y. Lee, H. Lee, M. Oh, Multi ball-in-ball hybrid metal oxides, Adv. Mater 23 (2011) 1720–1723.
[13] P. Arnal, M. Comotti, F. Schüth, High-temperature-stable catalysts by hollow sphere encapsulation, Angew. Chem. 118 (2006) 8404–8407.
[14] Y. Yin, R.M. Rioux, C.K. Erdonmez, S. Hughes, G.A. Somorjai, A.P. Alivisatos, Formation of hollow nanocrystals through the nanoscale Kirkendall effect, Science 304 (2004) 711–714.
[15] X.W. Lou, C. Yuan, E. Rhoades, Q. Zhang, L.A. Archer, Encapsulation and Ostwald ripening of Au and Au–Cl complex nanostructures in silica shells, Adv.

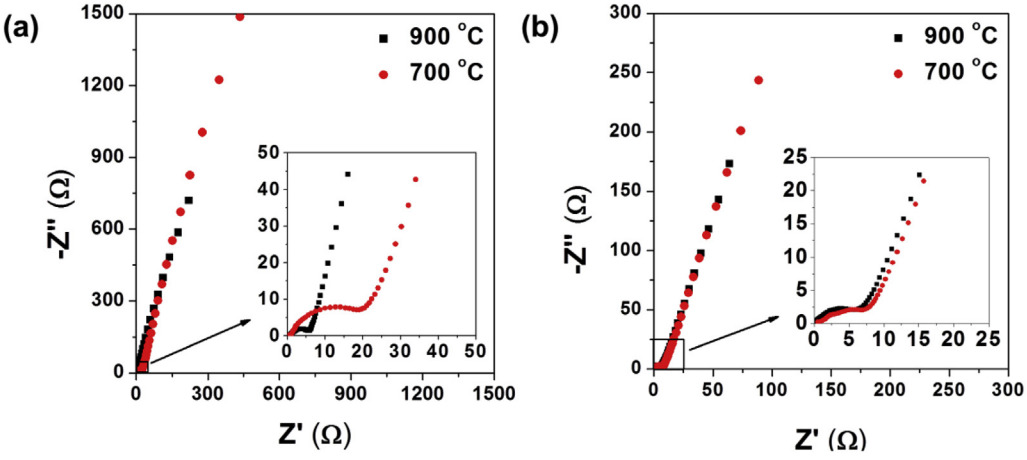

Fig. 6. - Nyquist plots of the powders prepared by spray pyrolysis at 700 and 900 °C: (a) before cycling and (b) after 50 cycles. (A color version of this figure can be viewed online.)

Funct. Mater 16 (2006) 1679–1684.
[16] J. Zhong, C. Cao, Y. Liu, Y. Li, W.S. Khan, Hollow core–shell η-Fe_2O_3 microspheres with excellent lithium-storage and gas-sensing properties, Chem. Commun. 46 (2010) 3869–3871.
[17] J.S. Chen, C.M. Li, W.W. Zhou, Q.Y. Yan, L.A. Archer, X.W. Lou, One-pot formation of SnO_2 hollow nanospheres and α-Fe_2O_3@SnO_2 nanorattles with large void space and their lithium storage properties, Nanoscale 1 (2009) 280–285.
[18] X.W. Lou, Y. Wang, C. Yuan, J.Y. Lee, L.A. Archer, Template-free synthesis of SnO_2 hollow nanostructures with high lithium storage capacity, Adv. Mater 18 (2006) 2325–2329.
[19] X.W. Lou, C.M. Li, L.A. Archer, Designed synthesis of coaxial SnO_2@carbon hollow nanospheres for highly reversible lithium storage, Adv. Mater 21 (2009) 2536–2539.
[20] Y.J. Hong, M.Y. Son, Y.C. Kang, One-pot facile synthesis of double-shelled SnO_2 yolk-shell-structured powders by continuous process as anode materials for Li-ion batteries, Adv. Mater 25 (2013) 2279–2283.
[21] Y.J. Hong, M.Y. Son, B.K. Park, Y.C. Kang, One-pot synthesis of yolk-shell materials with single, binary, ternary, quaternary, and quinary systems, Small 9 (2013) 2224–2227.
[22] S.H. Choi, J.K. Lee, Y.C. Kang, Controllable synthesis of yolk-shell-structured metal oxides with seven to ten components for finding materials with superior lithium storage properties, Nanoscale 6 (2014) 12421–12425.
[23] J.M. Won, S.H. Choi, Y.J. Hong, Y.N. Ko, Y.C. Kang, Electrochemical properties of yolk-shell structured $ZnFe_2O_4$ powders prepared by a simple spray drying process as anode material for lithium-ion battery, Sci. Rep. 4 (2014) 5857–5861.
[24] G.D. Park, J.H. Lee, J.K. Lee, Y.C. Kang, Effect of esterification reaction of citric acid and ethylene glycol on the formation of multi-shelled cobalt oxide powders with superior electrochemical properties, Nano Res. 7 (2014) 1738–1748.
[25] L. Zhou, H. Xu, H. Zhang, J. Yang, S.B. Hartono, K. Qian, J. Zou, C. Yu, Cheap and scalable synthesis of α-Fe_2O_3 multi-shelled hollow spheres as high-performance anode materials for lithium ion batteries, Chem. Commun. 49 (2013) 8695–8697.
[26] X. Wang, Y. Wang, L. Yang, K. Wang, X.W. Lou, B. Cai, Template-free synthesis of homogeneous yolk-shell TiO_2 hierarchical microspheres for high performance lithium ion batteries, J. Power Sources 262 (2014) 72–78.
[27] J. Liu, Y. Zhou, J. Wang, Y. Pan, D. Xue, Template-free solvothermal synthesis of yolk–shell V_2O_5 microspheres as cathode materials for Li-ion batteries, Chem. Commun. 47 (2011) 10380–10382.
[28] Z. Cai, L. Xu, M. Yan, C. Han, L. He, K.M. Hercule, C. Niu, Z. Yuan, W. Xu, L. Qu, K. Zhao, L. Mai, Manganese oxide/carbon yolk-shell nanorod anodes for high capacity lithium batteries, Nano Lett. 15 (2015) 738–744.
[29] J. Liu, H. Yang, F. Kleitz, Z. Chen, T. Yang, E. Strounina, G.Q. Lu, S.Z. Qiao, Yolk–Shell Hybrid materials with a periodic mesoporous organosilica shell: ideal nanoreactors for selective alcohol oxidation, Adv. Funct. Mater 22 (2012) 591–599.
[30] L. Liu, H. Guo, J. Liu, F. Qian, C. Zhang, T. Li, W. Chen, X. Yang, Y. Guo, Self-assembled hierarchical yolk–shell structured NiO@C from metal–organic frameworks with outstanding performance for lithium storage, Chem. Commun. 50 (2014) 9485–9488.
[31] Z.S. Wu, G.M. Zhou, L.C. Yin, W.C. Ren, F. Li, H.M. Cheng, Graphene/metal oxide composite electrode materials for energy storage, Nano Energy 1 (2012) 107–131.
[32] X. Zhou, Z. Dai, S. Liu, J. Bao, Y. Guo, Ultra-uniform SnO_x/carbon nanohybrids toward advanced lithium-ion battery anodes, Adv. Mater 26 (2014) 3943–3949.
[33] A. Mukhopadhyay, F. Guo, A. Tokranov, X.C. Xiao, R.H. Hurt, B.W. Sheldon, Engineering of graphene layer orientation to attain high rate capability and anisotropic properties in li-ion battery electrodes, Adv. Funct. Mater 23 (2013) 2397–2404.
[34] L. Zhang, G. Zhang, H.B. Wu, L. Yu, X.W. Lou, Hierarchical tubular structures constructed by carbon-coated SnO_2 nanoplates for highly reversible lithium storage, Adv. Mater 25 (2013) 2589–2593.
[35] X. Wang, X. Zhou, K. Yao, J. Zhang, Z. Liu, A SnO_2/graphene composite as a high stability electrode for lithium ion batteries, Carbon 49 (2011) 133–139.
[36] S. Choi, Y. Kang, Fe_3O_4-decorated hollow graphene balls prepared by spray pyrolysis process for ultrafast and long cycle-life lithium ion batteries, Carbon 79 (2014) 58–66.
[37] G. Zhou, D.W. Wang, F. Li, L. Zhang, N. Li, Z.S. Wu, L. Wen, G.Q. Lu, H.M. Cheng, Graphene-wrapped Fe_3O_4 anode material with improved reversible capacity and cyclic stability for lithium ion batteries, Chem. Mater 22 (2010) 5306–5313.
[38] G.M. Zhou, D.W. Wang, L. Li, N. Li, F. Li, H.M. Cheng, Nanosize SnO_2 confined in the porous shells of carbon cages for kinetically efficient and long-term lithium storage, Nanoscale 5 (2013) 1576–1582.
[39] L. Ji, Z. Lin, M. Alcoutlabi, X. Zhang, Recent developments in nanostructured anode materials for rechargeable lithium-ion batteries, Energy Environ. Sci. 4 (2011) 2682–2699.
[40] G. Zhou, D.W. Wang, L.C. Yin, N. Li, F. Li, H.M. Cheng, Oxygen bridges between NiO nanosheets and graphene for improvement of lithium storage, ACS Nano 6 (2012) 3214–3223.
[41] T. Wang, Z. Peng, Y. Wang, J. Tang, G. Zheng, MnO nanoparticle@mesoporous carbon composites grown on conducting substrates featuring high-performance lithium-ion battery, Supercapacitor Sens. Sci. Rep. 3 (2013) 2693–2701.
[42] Y. Xia, Z. Xiao, X. Dou, H. Huang, X. Lu, R. Yan, Y. Gan, W. Zhu, J. Tu, W. Zhang, X. Tao, Green and Facile Fabrication of Hollow porous MnO/C microspheres from microalgaes for lithium-ion batteries, Acs Nano 7 (2013) 7083–7092.
[43] L. Mai, F. Dong, X. Xu, Y. Luo, Q. An, Y. Zhao, J. Pan, J. Yang, Cucumber-Like V_2O_5/poly(3,4-ethylenedioxythiophene)&MnO_2 nanowires with enhanced electrochemical cyclability, Nano Lett. 13 (2013) 740–745.
[44] J.F. Moulder, W.F. Stickle, P.E. Sobol, K.D. Bomben, Handbook of X-ray Photoelectron Spectroscopy, in: J. Chastain (Ed.), Perkin-Elmer Corporation, Eden Prairie, MN, 1992.
[45] J.M. Themlin, M. Chtaib, L. Henrard, P. Lambin, J. Darville, J.M. Gilles, Characterization of tin oxides by X-ray-photoemission spectroscopy, Phys. Rev. B 46 (1992) 2460–2466.
[46] H. Kamari, M. Naseri, E. Saion, A novel research on behavior of zinc ferrite nanoparticles in different concentration of Poly(vinyl pyrrolidone) (PVP), Metals 4 (2014) 118–129.
[47] Y.J. Hong, Y.C. Kang, Formation of core–shell-structured Zn_2SnO_4–carbon microspheres with superior electrochemical properties by one-pot spray pyrolysis, Nanoscale 7 (2014) 701–707.
[48] R. Zhang, G. Fang, W. Liu, B. Xia, H. Sun, J. Zheng, D. Li, Preparation and electrochemical properties of core-shell carbon coated Mn–Sn complex metal oxide as anode materials for lithium-ion batteries, Appl. Surf. Sci. 292 (2014) 682–687.
[49] S. Lei, K. Tang, C. Chen, Y. Jin, L. Zhou, Preparation of Mn_2SnO_4 nanoparticles as the anode material for lithium secondary battery, Mater. Res. Bull. 44 (2009) 393–397.
[50] B. Sun, Z. Chen, H.-S. Kim, H. Ahn, G. Wang, MnO/C core–shell nanorods as high capacity anode materials for lithium-ion batteries, J. Power Sources 196 (2011) 3346–3349.
[51] Y. Sun, X. Hu, W. Luo, F. Xia, Y. Huang, Reconstruction of conformal nanoscale MnO on graphene as a high-capacity and long-life anode material for lithium ion batteries, Adv. Funct. Mater 23 (2013) 2436–2444.
[52] M.M. Rahman, J.Z. Wang, M.F. Hassan, D. Wexler, H.K. Liu, Amorphous carbon coated high grain boundary density dual phase $Li_4Ti_5O_{12}$-TiO_2: a nanocomposite anode material for Li-ion batteries, Adv. Energy Mater 1 (2011) 212–220.
[53] Y.P. Wu, E. Rahm, R. Holze, Carbon anode materials for lithium ion batteries, J. Power Sources 114 (2003) 228–236.
[54] X. Du, W. He, X. Zhang, Y. Yue, H. Liu, X. Zhang, D. Min, X. Ge, Y. Du, Enhancing the electrochemical performance of lithium ion batteries using mesoporous $Li_3V_2(PO_4)_3$/C microspheres, J. Mater. Chem. 22 (2012) 5960–5969.
[55] Y. Shi, J.Z. Wang, S.L. Chou, D. Wexler, H.J. Li, K. Ozawa, H.K. Liu, Y.P. Wu, Hollow structured Li_3VO_4 wrapped with graphene nanosheets in situ prepared by a one-pot template-free method as an anode for lithium-ion batteries, Nano Lett. 13 (2013) 4715–4720.